Article

Spin-reorientation driven emergent phases and unconventional magnetotransport in quasi-2D vdW ferromagnet Fe$_4$GeTe$_2$

Check for updates

Riju Pal [1] ✉, Buddhadeb Pal[1], Suchanda Mondal[2], Rajesh O. Sharma [3], Tanmoy Das[3], Prabhat Mandal[1] ✉ & Atindra Nath Pal [1] ✉

Non-trivial spin textures driven by strong exchange interaction, magneto-crystalline anisotropy, and electron correlation in a low-dimensional magnetic material often lead to unusual electronic transitions. Through a combination of transport experiments in exfoliated nanoflakes down to 16 layers and first principle calculations, we unravel emergent electronic phases in quasi-2D van der Waals ferromagnet, Fe$_4$GeTe$_2$, possessing ferromagnetic $T_C \sim 270$ K, along with a spin-reorientation transition ($T_{SR} \sim 120$ K) with the change of magnetic easy axis. Two electronic transitions are identified. The first transition near T_{SR} exhibits a sharp fall in resistivity, followed by a sign change in the ordinary Hall coefficient (R_0), together with, maximum negative magnetoresistance (MR) and anomalous Hall conductivity. Another unusual electronic transition, hitherto unknown, is observed near ~ 40–50 K (T_Q), where R_0 again changes sign and below which, the resistivity shows a quadratic temperature dependence, and MR becomes positive. An analysis of the experimental data further uncovers the role of competing inelastic scattering processes in anomalous magnetotransport behavior. The density-functional theory based first-principle calculations unveil two possible magnetic phases, followed by a low-energy model Hamiltonian which captures the essence of these phases as well as explains the observed magnetotransport behavior. Thus, we demonstrate an interplay between magnetism and band topology and its consequence on electron transport in Fe$_4$GeTe$_2$, important for spintronic applications.

The discovery of quasi-two-dimensional van der Waals (vdW) magnets[1–6] has opened up a new platform for investigating low-dimensional magnetism and its possible application in two-dimensional (2D) spintronic devices[7–10]. With the recent developments, the family of iron-based vdW magnets, like Fe$_n$GeTe$_2$ ($n = 3$, 4, 5) (FnGT)[11–27], especially Fe$_4$GeTe$_2$ (F4GT)[20–24] and Fe$_{5-x}$GeTe$_2$ (F5GT)[25–27], have attracted immediate attention due to their ferromagnetic transition temperature (T_C) close to room temperature. The Mermin-Wagner theorem[28] in the 2D limit dictates that there is no spontaneous magnetic order at finite temperature, but the uniaxial magneto-crystalline anisotropy stabilizes the long-range order in these vdW systems

against the thermal fluctuations. The enhanced T_C is achieved by increasing the exchange interaction as a result of the metal-rich unit cell[20,29,30]. However, the magnetism in these materials is rather complex in nature as compared to a typical ferromagnet, due to the presence of different inequivalent Fe atoms in the unit cell. For example, Fe$_3$GeTe$_2$ (F3GT) possesses antiferromagnetic order and non-collinear spin structure below 152 K[31], and also, unusual magnetic behavior was observed in F5GT at low temperature due to structural ordering of one of the Fe atoms in the unit cell at ~120 K[25]. More recently, it has been reported that bulk F4GT single crystal exhibits a change in easy axis of magnetization when cooled below ~120 K, termed as the

[1]Department of Condensed Matter and Materials Physics, S. N. Bose National Centre for Basic Sciences, Block JD, Sector III, Salt Lake, Kolkata 700106, India.
[2]Saha Institute of Nuclear Physics, HBNI, 1/AF Bidhannagar, Kolkata 700064, India. [3]Department of Physics, Indian Institute of Science, Bengaluru 560012, India.
✉e-mail: rijupal07@bose.res.in; prabhat.mandal@bose.res.in; atin@bose.res.in

'spin-reorientation transition' (SRT)[20,21], making it magnetically quite different from the other two family members. A similar SRT was observed in materials like Fe_3Sn_2[32–35], $Nd_2Fe_{14}B$[36], $TbMn_6Sn_6$[37–40], $LiMn_6Sn_6$[41], $NdCrSb_3$[42], $La_{0.4}Sm_{0.3}Sr_{0.3}MnO_3$[43] etc. The interplay between magnetic exchange and effective magnetic anisotropy is possibly the reason for this spin-reorientation[20,22,44]. The recent transport measurements indicate that the SRT may lead to Lifshitz transition in the electronic structure, and as a result, the system may exhibit unusual magnetotransport and anomalous Hall effect (AHE)[41,45]. While in the case of F4GT, an anomaly in the specific heat was seen, indicating that it is indeed a thermodynamic phase transition[22], its consequence on electron transport is still elusive.

Besides the unusual magnetic properties, electronically these materials possess interesting features. All the members of the FnGT family are predicted to be semimetal as the density-functional theory (DFT)-based calculations show multiple band crossing at the Fermi level[46,47]. More importantly, the presence of different crystal symmetry and the spin-orbit coupling (SOC) may suggest a topologically non-trivial phase with unusual effects induced by the chiral anomaly like negative magnetoresistance (MR) or nonlinear conductivity in the diffusive limit[14]. Furthermore, the broken time-reversal symmetry (TRS) in these topological phases hints at a more exotic ground state leading to observations like large intrinsic AHE (in F3GT)[48] or unusual magnetotransport behavior at low temperatures[49]. These systems often exhibit non-monotonic transport features correlated with temperature-dependent magnetization[50]. While the low-temperature transport is relatively easy to address as the effect of inelastic electron-phonon or electron-magnon interactions is negligible compared to the intrinsic effect, the role of these competing interactions on the transport behavior at intermediate or high temperatures is not fully established[51].

Here, we study the temperature-dependent electronic and magneto-transport behavior of F4GT single crystal in detail. A single layer of F4GT consists of seven atoms (Fe_1 and Fe_2 arranged on both sides of the Ge atomic plane, and they are connected with Te atoms directly on both sides), as shown in Fig. 1a. The stacking of these F4GT monolayers forms a rhombohedral structure with space group $R\bar{3}m$[20]. Electronically this has been predicted to be a different class with non-trivial topology, unlike F3GT or F5GT[46,47]. Single crystal of F4GT was prepared by the chemical vapor transport (CVT) methods exhibiting the ferromagnetic $T_C \sim 270$ K where the dM/dT shows the minimum, followed by the SRT at $T_{SR} \sim 120$ K below which the magnetization along out-of-plane direction becomes larger than that of its in-plane value (see Fig. 1b). By fabricating multilayer Hall bar devices on predefined Ti/Au contacts using the dry-transfer method (see Fig. 1c for the schematic of the device and Supplementary Note 1 and 2 for details about the crystal preparation and device fabrication), we studied the temperature-dependent resistivity, MR, and Hall effect from room temperature (300 K) down to 1.6 K. In particular, we observe the direct consequences of the SRT on the charge conduction mechanism, leading to the change in the majority carrier types, confirmed by the temperature-dependent ordinary Hall coefficient. Remarkably, a sharp decrease in resistivity followed by the enhanced negative MR and the maximum anomalous Hall conductivity were observed near the SRT. While the analysis of resistivity data uncovers the role of different inelastic scattering mechanisms like electron-electron, electron-magnon, and electron-phonon interaction in the different temperature ranges, we find that electron-magnon scattering is also responsible for the temperature-dependent MR and AHE. Finally, we report an electronic transition (T_Q) occurring near ~ 40–50 K, below which, the resistivity shows a quadratic temperature
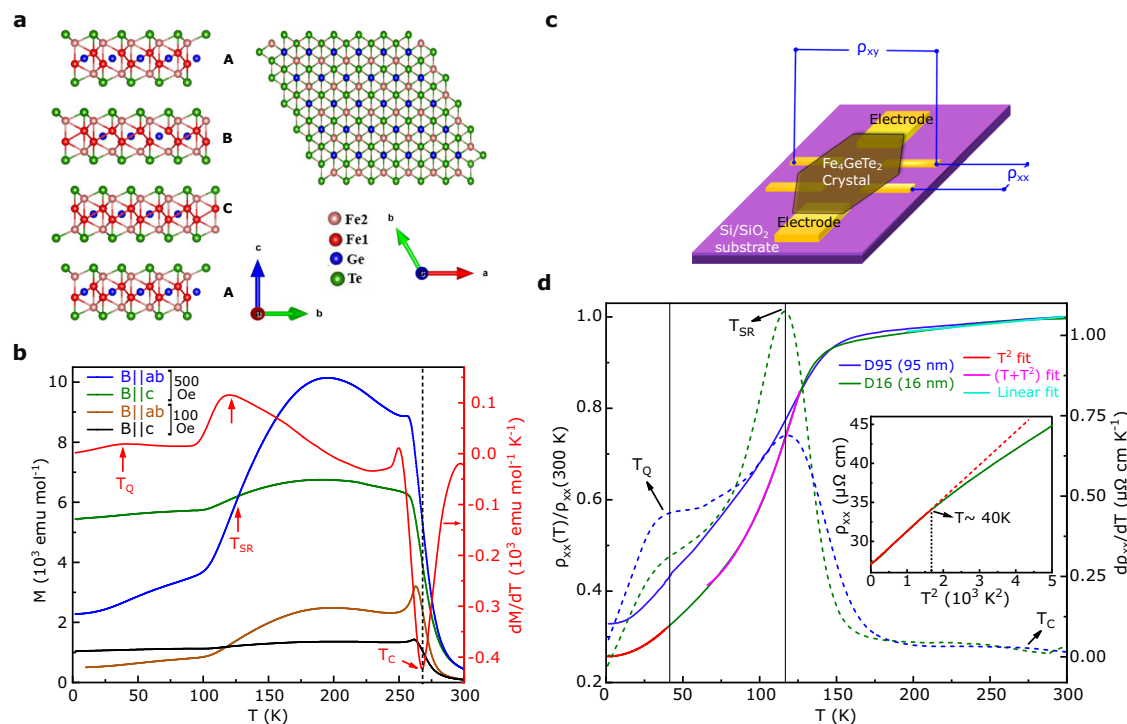

Fig. 1 | Crystal structure, temperature-dependent magnetization and resistivity. a Schematic diagram of the structure of F4GT crystal: side view (left) and the top view (right). Seven atom thick F4GT monolayers are arranged in the ABC configuration, leading to the formation of the rhombohedral structure with the space group $R\bar{3}m$. **b** The dc magnetization data as a function of temperature are plotted with applied field 500 Oe and 100 Oe along B ‖ ab and B ‖ c of the crystallographic axis of F4GT crystal, measured in zero-field-cooled (ZFC) condition. The red curve shows the temperature derivative of the magnetization (dM/dT) data of 500 Oe with B ‖ ab plane, indicates three transitions, Curie temperature (T_C) ~270 K, the spin-reorientation transition (T_{SR}) at around 120 K, and a small kink (T_Q) near ~40 K.

c Schematic diagram of six terminal Hall-bar electrodes with transferred F4GT multilayer crystal for low-temperature magnetotransport measurements. **d** Temperature dependence of the normalized zero-field electrical resistivity (ρ_{xx}) curves for two different nanoflake devices with thicknesses 95 nm (D95, blue) and 16 nm (D16, green). The corresponding temperature derivatives of resistivity for both devices are shown by the blue and green dotted curves, respectively. Here, the current is applied to the in-plane direction (I ‖ ab plane). Theoretical fits to the temperature dependence of zero-field resistivity data of D16 at different temperature ranges are indicated with red, purple, and cyan colors. Inset: ρ_{xx} vs T^2 curve shows a clear change of slope above ~40 K.
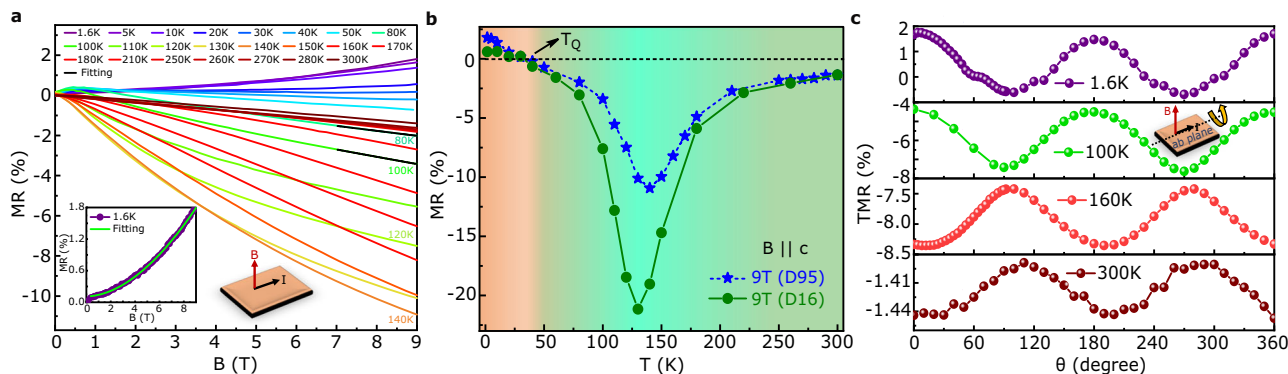
Fig. 2 | Magnetoresistance at different temperatures. a Magnetic field dependence of magnetoresistance (MR) measured from temperature 1.6 K up to 300 K. Here, the external magnetic field is applied parallel to the *c* axis and the current is in the ab plane of the F4GT sample (D95). Black lines are the fitting of Eq. (4) at 80 K and 100 K. Inset: low-temperature (1.6 K) MR is fitted with Eq. (3). Fitting results provide the value of the parameters, $\mu = 0.147$ m^2 V^{-1} s^{-1} and $n = 1.847$. **b** Temperature dependence of MR is plotted for two devices with applied field 9 T along the c-axis of the crystal, indicating a maximum negative MR at around T_{SR} and a small positive MR below T_Q. Background colors indicate two different regimes, positive and negative MR. Color contrast signifies the magnitude of MR. **c** Angle-dependent transverse magnetoresistance (TMR) at 9 T at different temperatures shows a definite spin-reorientation between 100 K and 160 K, and it confirms the anisotropic behavior of the crystal.

dependence, consistent with Fermi-liquid behavior, along with a weak positive MR. All the above experimental results were verified and compared to elucidate the electronic properties in the thin limit using two distinct exfoliated devices with thicknesses of ~95 nm (D95) and ~16 nm (D16). DFT-based first principle calculations unravel two quasi-degenerate magnetic phases, collinear FM (cFM) and non-collinear FM (nFM), which are associated with the SRT. The electronic structures and fermiologies of the two magnetic phases also reveal Fermi surface (FS) reconstruction near this transition. Motivated by the DFT result, a two-channel Heisenberg Hamiltonian is introduced to explain the SRT in F4GT.

Results and discussion
Resistivity
Figure 1d shows the temperature-dependent normalized in-plane resistivity (ρ_{xx}) of two Hall bar devices D95 and D16, fabricated on 285 nm Si/SiO$_2$ substrate (see Methods section and Supplementary Note 2 for details), both measurements were done with a constant ac excitation of 50 μA at zero magnetic field. ρ_{xx} exhibits a metallic behavior, with almost negligible change near the FM transition. However, the resistivity falls dramatically near SRT. ρ_{xx} shows a weak anomaly near T_Q (~40 K), indicated by a clear kink in the $d\rho_{xx}/dT$ curves (blue and green dotted line in Fig. 1d), whose consequence on the transport will be discussed. The residual resistivity ratio (RRR = ρ_{xx}(300 K)/ρ_{xx}(1.6 K)) values of both the exfoliated devices are 3.87 (D16) and 3.04 (D95), while the corresponding absolute conductivity (σ) at T_C (~270 K) are ~9.6×10^5 Ω^{-1} m^{-1} (D16) and ~8.6×10^5 Ω^{-1} m^{-1} (D95), being relatively higher compared to several other 2D ferromagnets[6,14,52] and consistent with the reported value for this material[20]. Comparatively, a higher conductivity is observed for the thinner device (D16) at the lowest temperature (1.6 K), indicating enhancement of metallicity at reduced thicknesses. This observation also aligns with the findings from earlier reports[20].

According to Matthiessen's rule, the total resistivity of a metallic ferromagnet consists of all the contributions coming from various scattering mechanisms and they are additive within each conduction band[53,54]. The temperature dependence of longitudinal resistivity can be written as:

$$\rho_{xx}(T) = \rho_0 + \rho_{e-p}(T) + \rho_{e-e}(T) + \rho_{e-m}(T, B) \quad (1)$$

where ρ_0 is the residual resistivity arising due to the temperature-independent elastic scattering from the static defects. ρ_{e-p}, ρ_{e-e}, and ρ_{e-m} are the inelastic electron-phonon, electron-electron, and electron-magnon scattering contributions, respectively. Among these, ρ_{e-p} varies linearly with temperature ($\propto T$), and both ρ_{e-e} and ρ_{e-m} exhibit quadratic behavior with

temperature ($\propto T^2$). As the electron-magnon term is strongly dependent on the magnetic field, whereas, other terms remain insensitive, the field-dependent resistivity can be used to identify the actual mechanism.

It is clear from Fig. 1d that the nature of the temperature dependence of resistivity is extremely sensitive to temperature regions. At low temperatures below ~40 K, ρ_{xx} follows a perfectly quadratic behavior ($\rho_{xx} \propto T^2$), corresponding to either electron-electron (e-e) scattering or electron-magnon (e-m) scattering. To identify the actual mechanism, we measured the temperature-dependent resistivity at a high magnetic field (9 T) in both the in-plane and out-of-plane direction of the crystal (See Supplementary Note 4 and Supplementary Fig. 6). It is observed that the resistivity is almost independent of the magnetic field, which suggests that the dominant scattering mechanism is indeed the electron-electron interaction, confirming Fermi-liquid behavior. The magnitude of the coefficient of the quadratic term is the measure of the electron-electron scattering rate. Focusing on D16, we found the value of this coefficient to be 4.24×10^{-9} Ω cm K^{-2}, which is nearly two orders of magnitude larger than the elemental ferromagnets like Fe, Co, and Ni, but comparable to the value of the semi-metals like Bi, graphite, etc.[55–60]. In the intermediate range (65–125 K), ρ_{xx} can be fitted with the admixture of both linear and quadratic contributions i,e. $\rho_{xx} = \rho_{xx}(T, T^2)$. While the linear dependence corresponds to the electron-phonon coupling, the T^2 dependence signifies the electron-magnon scattering. This is evident from the fact that the resistivity has a strong dependence on the magnetic field in this regime and the coefficient of the T^2 term is reduced significantly at a high magnetic field (see Supplementary Note 4). Also, it is important to note that the electron-magnon scattering strength is larger by a factor of four for D16 compared to D95 (see Table 2). At high temperatures ($T > 190$ K), well above the SRT, a complete linear dependence of resistivity on temperature is observed ($\rho_{xx} \propto T$), indicating the dominance of the electron–phonon scattering mechanism. A similar analysis is consistent for the device D95, as discussed in Supplementary Note 8.

Magnetoresistance
We next concentrate on the temperature dependence of MR. Figure 2a shows the MR [=(($\rho_{xx}(B)-\rho_{xx}(0))/\rho_{xx}(0)$) × 100%] at different temperatures starting from 300 K down to 1.6 K with the applied magnetic field along the out-of-plane direction (c-axis) of the F4GT crystal (D95) (For D16, see Supplementary Fig. 7). In order to eliminate the contribution from the Hall resistance due to a small misalignment of the electrodes, we symmetrize the data using the expression, $\rho_{xx}(B) = (\rho_{xx}(+B) + \rho_{xx}(-B))/2$. The high-field (9 T) MR (Fig. 2b) exhibits several interesting features. MR is predominantly negative in the range between ~40 K to 300 K, and its value is maximum near the SRT, being ~11% for D95 and ~21.2% for D16 (see Fig. 2b). As the

thinner device is more suspectable to electron-magnon scattering (see Table 2), the application of magnetic field suppresses the resistance more in the case of the thinner device, providing greater negative MR. Below T_Q, MR is small but positive (~1.8% for D95 and 0.6% for D16 at 1.6 K), quite unusual for a metallic ferromagnet. To test whether the electronic properties are isotropic or not, the angle-dependent transverse magnetoresistance (TMR) measurements at 9 T are performed at different temperatures, as shown in Fig. 2c. While the low-temperature data below 100 K show cosine-like behavior, it shows a phase shift by 90 degrees above the T_{SR}, depicting the easy axis change from the c axis to the ab-plane with increasing temperature (See Supplementary Fig. 10 for plots near SRT).

In general, the resistivity of a ferromagnetic material can be expressed as a function of the electronic relaxation time (τ) and its field dependence as[61,62],

$$\rho_{total} = k_1(\omega_c\tau)^n + k_2(1/\tau) \tag{2}$$

where, ω_c is the cyclotron frequency of the free carriers. Here, the first term is the orbital contribution to the resistivity arising due to the constrained orbital motion of the free carriers under the Lorentz force and responsible for positive MR. The second term describes the contributions from the various scattering mechanisms as explained in Eq. (1). The field dependence of the orbital term can be expressed as,

$$\rho_{orb} \propto (\omega_c\tau)^n = (\mu B)^n \tag{3}$$

where μ is the mobility of the free carriers. Ideally, for a nonmagnetic metal, the exponent $n = 2$[63], but for other systems like doped semiconductors[64], ferromagnetic metallic thin films[53], spin-glass systems[65], etc., its value deviates from 2 and lies in between 1 and 2 ($1 < n < 2$). By fitting the positive MR at low temperature, we observe that the exponent n is close to 2 (See Fig. 2a inset, Supplementary Note 5 and Supplementary Fig. 9 for fitting), being closer to the behavior of a typical metal having pure orbital contribution.

At higher temperatures above T_Q, we have observed a crossover in MR from positive to negative (see Fig. 2a) and its value becomes maximum near the SRT. The enhanced MR is associated with the dominance of electron-magnon scattering in this intermediate range, due to the strong coupling between charge and spin degrees of freedom driven by the SRT.

The role of electron-magnon scattering on negative MR in a ferromagnet has been discussed in ref. [53] and an analytical expression is given, which is valid for magnetic field below 100 T and in the temperature range of $T_C/5$ to $T_C/2$,

$$\Delta\rho_{xx}(T, B) \propto \frac{BT}{D(T)^2} \ln\left(\frac{\mu_B B}{k_B T}\right) \tag{4}$$

where, $D(T)$ is the magnon stiffness or magnon mass renormalization constant, μ_B is the Bohr magneton and k_B is the Boltzmann constant. The high-field MR data ($B > 7$ T) above 50 K in the temperature range 80 K and 100 K ($T_C/5 < T < T_C/2$) can be well-fitted with Eq. (4) (see Fig. 2a), confirming that the non-saturated negative MR is originated primarily due to the suppression of electron-magnon scattering under the external magnetic field.

Hall Measurements

Now, we focus on the Hall effect in F4GT. Typically, the Hall resistivity (ρ_{xy}) of a ferromagnetic material can be described by an empirical formula[66,67],

$$\rho_{xy} = \rho_{xy}^{OHE} + \rho_{xy}^{AHE} = R_0 B + \mu_0 R_S M \tag{5}$$

Here, the first term is the ordinary Hall resistivity (ρ_{xy}^{OHE}) and the second term represents the anomalous Hall resistivity (ρ_{xy}^{AHE}). From the magnitude of the ordinary Hall coefficient, R_0, one can calculate the effective carrier concentration when a single band picture is valid, and its sign determines the type of majority carriers present in the material. On the

other hand, the anomalous Hall part is proportional to the spontaneous magnetization (M) and the proportionality constant, R_S, is defined as the anomalous Hall coefficient. In most ferromagnets, as the magnetization saturates well below T_C above some critical field, ρ_{xy} varies linearly with B. From the linear fitting of ρ_{xy} in the high-field regime, one can obtain R_0 from the slope and the anomalous Hall resistivity (ρ_{xy}^{AHE}) from the intercept. Also, the anomalous Hall coefficient, R_S, can be calculated by using the relation, $\rho_{xy}^{AHE} = \mu_0 R_S M_S$, where M_S can be extracted from the M–B curves (see Fig. 3a) above $B \geq 7$ T.

However, the above-mentioned technique is not applicable when the magnetization does not saturate at a high field as can be seen from the M–B plots (see Fig. 3a, Supplementary Note 3 and Supplementary Fig. 5). We observe that the magnetization does not show complete saturation as T approaches T_{SR} even till $B = 9$ T (see Fig. 3a). To circumvent the problem, we incorporate the field dependence of magnetization in Eq. (5) and use the modified equation for fitting as,

$$\frac{\rho_{xy}}{B} = R_0 + \mu_0 R_S \frac{M}{B} \tag{6}$$

From the fitting, we can determine the values of R_S and R_0. Both methods qualitatively provide equivalent results except some quantitative differences in the high-temperature range. Details of calculation procedures are explained in Supplementary Note 6.

Figure 3b demonstrates the magnetic field-dependent Hall resistivity (ρ_{xy}) for D16 measured at different temperatures down to 10 K (for D95, see Supplementary Fig. 15). Here, the similarity in the nature of magnetic field dependence curves of Hall resistivity and magnetization in the low-field region suggests the presence of AHE.

We first discuss the behavior of temperature dependence of the ordinary Hall coefficient, R_0, which shows a rather complex nature. Figure 3c shows that R_0 changes sign from positive (red) to negative (blue) in the proximity of T_{SR}, reaching its maximum negative value at ~T_{SR} and becomes positive again in the vicinity of ~T_Q. Almost identical behavior was observed in both of the devices, D95 and D16. This indicates the change in the majority carrier from holes to electrons, possibly due to the FS reconstruction or Lifshitz-like transition occurring as a result of the SRT[41,45], however, the actual origin is not yet known. We compare the observed behavior of R_0 for F4GT with the reported result[48] on F3GT. Unlike F4GT, the slope of the Hall resistivity (R_0) in F3GT is positive from 2 K to 300 K, indicating the hole-dominating majority carrier throughout this temperature range[48]. Nevertheless, the Hall resistivity clearly demonstrates a strong correlation between spin structure and the FS, which leads to the non-monotonic temperature dependence of R_0[68] in F4GT down to 16 layers.

The temperature-dependent anomalous Hall coefficient (R_S) for D16, derived using Eq. (6), is shown in Fig. 3d. R_S shows a non-monotonic behavior with its maximum at ~140 K and a strong decrease below the SRT. However, it was argued that the R_S may not describe the proper scaling with M when there is a significant variation in resistivity with T or B and a material-specific scaling factor S_H was introduced where $R_S = S_H\rho_{xx}^2$[69]. Figure 3d (red curve) shows the variation of S_H with temperature, which shows a weak variation with the temperature well above the SRT transition and changes significantly below SRT, indicating its complex dependence with resistivity and magnetism below the SRT. A nearly identical behavior is noticed for device D95 with the distinction lying in its enhanced values at elevated temperatures (see Supplementary Notes 9 and 10 for the comparisons between D16 and D95).

To investigate the origin of the AHE, typically one looks at the scaling behavior of ρ_{xy}^{AHE}, $\rho_{xy}^{AHE} \approx a\rho_{xx}^\alpha$[70]. Primarily three mechanisms were identified to describe the AHE for ferromagnets or materials with strong spin-orbit coupling (SOC): intrinsic Karplus–Luttinger (K-L) mechanism, extrinsic side-jump mechanism, and extrinsic skew-scattering mechanism[70]. Intrinsic K-L mechanism[71] is associated with the anomalous drift of carriers due to the finite Berry curvature in the momentum space appearing due to the SOC. It is mostly independent of scattering and solely dependent on the
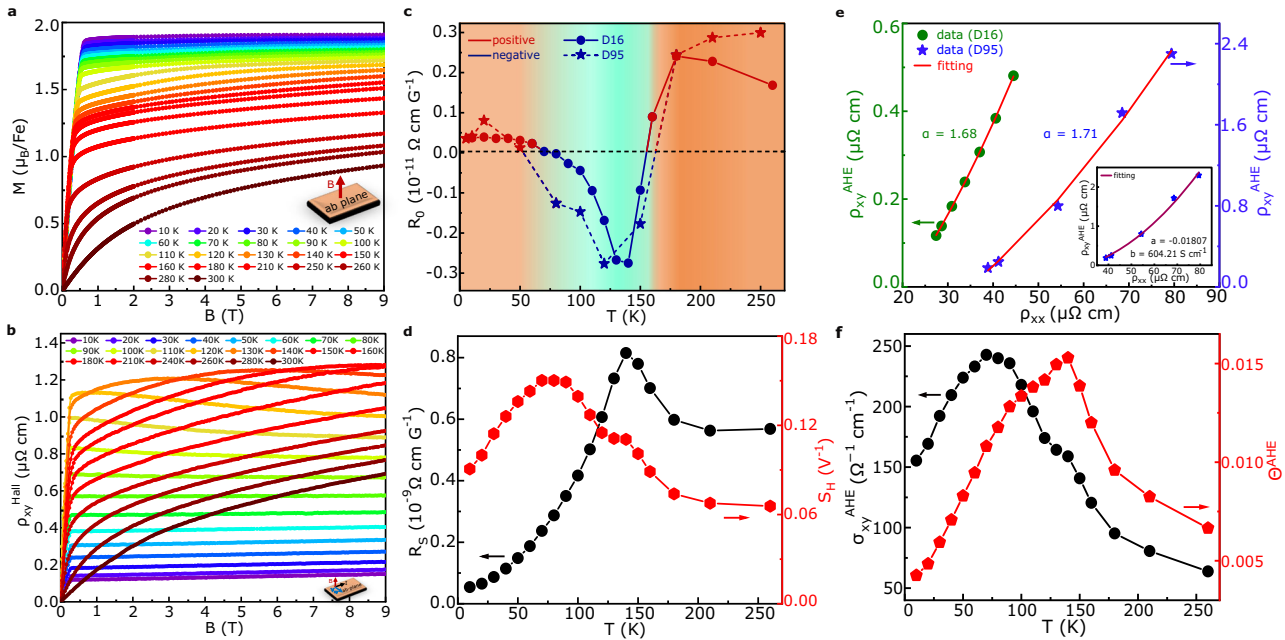
Fig. 3 | Temperature-dependent magnetization and Hall effect with analysis.
a Magnetic field dependence of magnetization (M) at different temperatures with B normal to the ab-plane of the crystal. **b** Magnetic field dependence of Hall resistivity (ρ_{xy}) of D16 measured at temperatures from 10 K to 300 K, with current in ab-plane and magnetic field along the c-axis of the F4GT crystal. **c** Temperature dependence of the ordinary Hall coefficient (R_0) for the two devices (D16 and D95), indicating both positive and negative regimes through the background colors. **d** Temperature dependence of anomalous Hall coefficient R_S and scaling coefficient $S_H = R_S/\rho_{xx}^2 =$ $-\sigma_{xy}^{AHE}/M$ are plotted for device D16. **e** Scaling behavior of anomalous Hall resistivity (ρ_{xy}^{AHE}) vs in-plane resistivity (ρ_{xx}) for both devices. The red curve indicates the fitting of the experimental data with the equation $\rho_{xy}^{AHE} \approx a\rho_{xx}^\alpha$, which helps to understand the origin of the anomalous Hall effect. Inset: the data (D16) are fitted with the equation $\rho_{xy}^{AHE} = a\rho_{xx} + b\rho_{xx}^2$. **f** Temperature dependence of anomalous Hall conductivity (σ_{xy}^{AHE}) provides a larger value of 243 Ω^{-1} cm^{-1} at 80 K for device D16. Temperature dependence of anomalous Hall angle $\theta^{AHE} = \sigma_{xy}^{AHE}/\sigma_{xx}$ has an anomaly near the spin-reorientation transition (T_{SR}).

band structure of the crystal[70,72,73]. Extrinsic side-jump mechanism[74] is related to the deflection of electrons due to scattering from the spin-orbit coupled impurities, and extrinsic skew-scattering mechanism[75,76] is caused by the asymmetric scattering of electrons from the impurities due to the spin-orbit interactions. All of these three mechanisms are associated with the power-law, $\rho_{xy}^{AHE} \approx a\rho_{xx}^\alpha$. For intrinsic K-L mechanism and extrinsic side-jump mechanism $\alpha = 2$ and for extrinsic skew-scattering mechanism $\alpha = 1$ [70].

To get a quantitative estimate, we have calculated the anomalous Hall conductivity ($|\sigma_{xy}^{AHE}| \approx \rho_{xy}^{AHE}/\rho_{xx}^2 \approx \mu_0 R_S M_S/\rho_{xx}^2$) and the anomalous Hall angle ($\theta_{AHE} = \sigma_{xy}^{AHE}/\sigma_{xx}$), which is a measure of the strength of the transverse current generated with respect to the applied normal current[70]. It must be noted that the anomalous Hall conductivity is overestimated at the higher temperatures ($T > T_{SR}$) as M does not show full saturation even with 9 T magnetic field (see Fig. 3a). The temperature dependence of $|\sigma_{xy}^{AHE}|$ and θ_{AHE} exhibit a non-monotonic behavior, as shown in Fig. 3f (for D16). While at low temperature (10 K), $|\sigma_{xy}^{AHE}| \approx 155\,\Omega^{-1}$cm^{-1}, it increases and attains a maximum value of ~243 Ω^{-1} cm^{-1} at ~80 K, then decreases with increasing temperature. In case of D95, a similar non-monotonic temperature-dependent behavior is observed, with $|\sigma_{xy}^{AHE}| \approx 121\,\Omega^{-1}$cm^{-1} at 10 K and a relatively higher maximum value of ~376 Ω^{-1} cm^{-1} at ~80 K (see Supplementary Note 9 for detail comparison). For thinner nanoflake device, D16, θ_{AHE} and S_H reach the values of ~0.015 and ~0.15 V^{-1} respectively, near T_{SR} (see Fig. 3d, f). The corresponding values for D95 are ~0.032 and ~0.24 V^{-1}, respectively (see Supplementary Fig. 16). These results are quite high among these classes of 2D ferromagnetic materials at such higher temperatures, especially in devices with lower thicknesses[14,77].

The low-temperature value is almost three times smaller than the expected AHE conductivity in the 'resonant' condition, ~$e^2/ha \approx 390\,\Omega^{-1}$ cm^{-1}[14,73] in three dimensions, where e is the electronic charge, h is the Planck constant and $a = 9.97$ Å [20], being the lattice constant of F4GT. Also, the recent DFT-based calculations

show that F4GT belongs to a different magnetic symmetry class compared to the other two members, having a non-trivial Berry curvature leading to the low-temperature AHE conductivity via intrinsic K-L mechanism[46]. However, the strong temperature dependence of the AHE suggests that extrinsic mechanisms might play a role in determining the AHE in F4GT. The extrinsic side-jump contribution to the AHE conductivity (σ_{xy}^{AHE}) is of the order of $e^2/(ha)(\varepsilon_{SO}/E_F)$ [78], where ε_{SO} is the spin-orbit coupling interaction and E_F is the Fermi energy. While for ferromagnetic metals, the ratio, ε_{SO}/E_F is usually small (~0.01) and so the extrinsic side-jump contribution[14,32], it may enhance due to the complex nature of magnetic interaction in this class of van der Waals ferromagnets.

It is hard to identify the exact mechanism responsible for AHE due to the observed strong temperature dependence of the AHE coefficient below the SRT. The theory of AHE does not include the role of inelastic scattering like electron-electron, electron-magnon, or electron-phonon interaction. As both our resistivity and MR data indicate a dominant electron-magnon scattering in the intermediate temperature range, the AHE might also have a similar origin. First, ρ_{xy}^{AHE} vs ρ_{xx} is plotted to check the scaling behavior of ρ_{xy}^{AHE} of both devices (D16 and D95) in the temperature range from 5 K to 100 K, as shown in Fig. 3e. From the fitting (red curve in Fig. 3e) of the equation $\rho_{xy}^{AHE} \approx a\rho_{xx}^\alpha$, we have determined the values of $\alpha = 1.68$ (for D16) and 1.71 (for D95), i.e., almost quadratic dependence of ρ_{xy}^{AHE} on ρ_{xx}, which indicates that the AHE of F4GT could be originated dominantly from the intrinsic K-L mechanism or extrinsic side-jump mechanism, rather than the extrinsic skew-scattering mechanism where ρ_{xy}^{AHE} linearly dependent on ρ_{xx}. To understand the dominant contributions, we have plotted ρ_{xy}^{AHE} with ρ_{xx} (inset of 3e for D95, see Supplementary Fig. 8 for D16) and fitted with the equation $\rho_{xy}^{AHE} = a\rho_{xx} + b\rho_{xx}^2$, where a is the strength of skew-scattering contribution and b denotes the strength of the side jump/intrinsic contribution. From the fitting, we estimate $a = -0.0181$ and $b \sim 604$ S cm^{-1}, which indicates that the intrinsic Berry phase and/or extrinsic side-jump
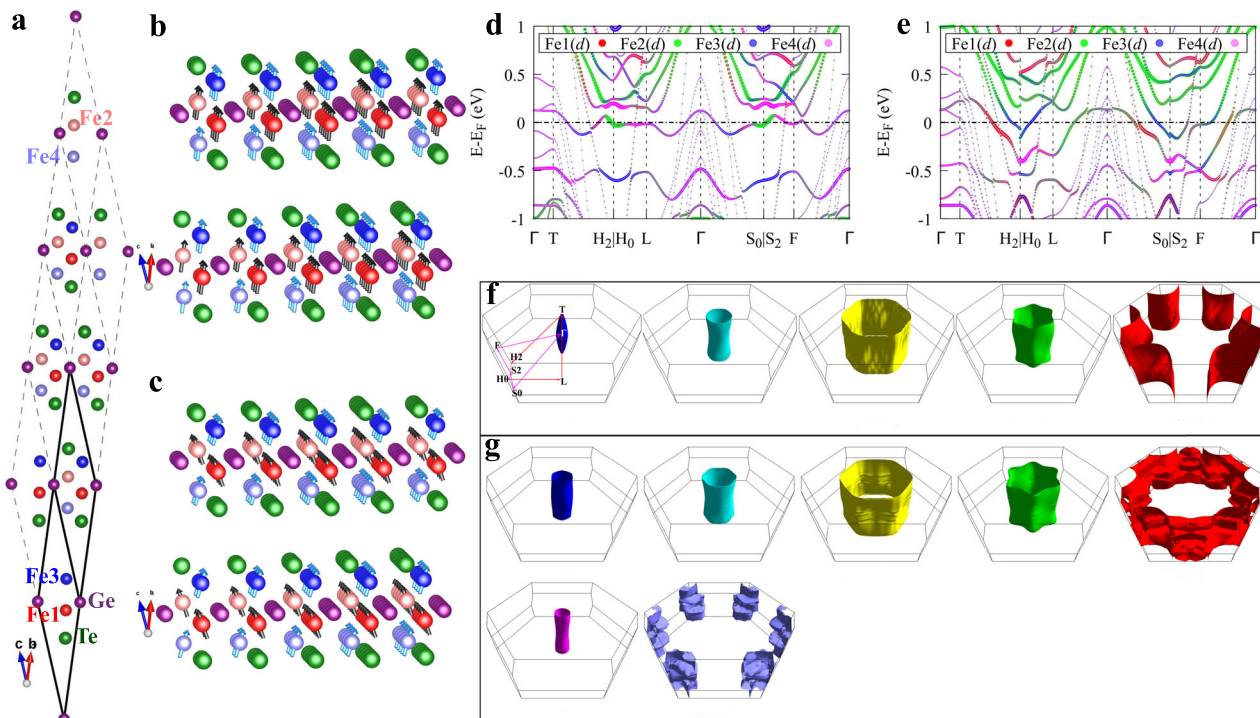
Fig. 4 | Results from theoretical calculations. a A 2×2 supercell is constructed using the Rhombohedral primitive cell (depicted by the solid line) of the F4GT compound. Four Fe atoms are labeled as Fe1, Fe2, Fe3, and Fe4 in different colors. **b** The cFM phase with all Fe atoms having magnetic moments along the ab-plane, as indicated by black (Fe1-Fe2) and cyan (Fe3-Fe4) arrows. Only two layers, each composed of Fe, Ge, and Te, from the 4×4 supercell are displayed here for simplicity. **c** In the nFM phase, the magnetic moments of all Fe atoms are shown reoriented and shown by corresponding arrows. **d, e** The projected band structure is shown in the cFM and nFM phases. We also plot the total d orbital weights of all four Fe atoms, with the thickness of the line indicating the orbital weight while different color reflects different Fe atoms. **f, g** Corresponding Fermi surfaces in the two phases are drawn here. Here color has no physical meaning except to distinguish different bands.

contribution highly dominate over the skew-scattering contribution. Here, the negative sign of a indicates that the skew-scattering contribution is acting in the opposite direction as compared to the other two mechanisms[51,79].

Since the extrinsic side-jump contribution is independent of the strength and density of the scatters similar to intrinsic mechanisms and both of them follow the quadratic dependence to the longitudinal resistivity ($\propto \rho_{xx}^2$), it is difficult to separate the intrinsic K-L and extrinsic side-jump contributions. Usually, the intrinsic part does not change with temperature in most cases unless there is an electronic transition with temperature leading to non-monotonic Berry phase contribution[70,80]. Recently, Yang et al.[81] theoretically proposed that the side-jump contribution can be affected by the electron-magnon scattering, which may lead to the temperature dependence of anomalous Hall conductivity (AHC). To investigate further, we decouple different scattering terms of $R_S(T)$ using the procedure mentioned in refs. [51,54,79,81] (for detailed calculations, see Supplementary Note 7). Supplementary Fig. 13 shows the temperature dependence plot of change in resistivity ($\Delta\rho_{xx}$) at 9 T magnetic field and the extrinsic side-jump contribution, R_S^{SJ}. The red line shows the extracted side jump contribution to the resistivity, which scales perfectly in the temperature range $T_Q < T < T_{SR}$, but deviates in the low-temperature regime ($T < T_Q$) as well as for $T > T_{SR}$. Additionally, R_S^{SJ} also shows a linear relation with $|\Delta\rho_{xx}|_{9T}$ (see the inset in Supplementary Fig. 13). The analysis directly indicates that the $R_S^{SJ}(T)$ primarily originates from the spin-flip electron-magnon scattering. The above analysis is also consistent with the observed reduction in the AHE conductivity near T_{SR} for the thinner layer device (see Supplementary Fig. 16). As the observed electron-magnon scattering coefficient deduced from the resistivity data is higher for thinner flake, it leads to the enhanced side jump contributions[82,83] which further reduces the AHE conductivity near T_{SR} for thinner layer device, consistent with the above analysis.

First principle study of Fe$_4$GeTe$_2$

It is one of the outstanding puzzles in this material class that despite strong ferromagnetic transitions (nearly reaching room temperature), the materials' charge degrees of freedom are not frozen and the material behaves as a ferromagnetic metal. Moreover, the above experimental results clearly indicate that within the ferromagnetic phase, there are multiple phase transitions–with lowering the temperature, there exists a spin reorientation (SR) transition (at T_{SR}), while another electronic phase transition occurs at a much lower temperature T_Q giving a Fermi-liquid-like behavior. A ferromagnetic metal suggests a Hubbard model as a starting Hamiltonian, while the SR phase suggests an anisotropic Heisenberg coupling term, and the electronic phase transition within a magnet entails a Kondo coupling. After delineating the electronic properties within the DFT calculation, we propose a low-energy model Hamiltonian to capture the essence of these phases.

We first present the results from the DFT calculation in two nearly degenerate magnetic configurations, as shown in Fig. 4. The details of the DFT calculation are given in the Methods section and Supplementary Note 11. The Fe$_4$GeTe$_2$ compound has two well-separated quarter-layers of Fe, in which two pairs of equivalent Fe atoms reside as Fe1, Fe2 and Fe3, Fe4. Due to van der Waals interaction between these quarter-layers, and hence having negligible exchange interaction between their spins, we can essentially focus on a given quarter-layer. The energy optimization within the non-collinear DFT+U calculation yields two FM configurations which are nearly 10 meV (see Table 1). The lowest energy configuration is a collinear ferromagnet, with an easy axis pointing along the ab-plane for all Fe atoms. In the other phase, there is a relative tilt (~60°) between the spin easy axes of the two Fe atoms, with the overall spin orientation also nearly 40° from the c-axis. Experimentally, the spin orientation is nearly 90°, and this difference between theory and experiment could be related to the global spin-rotational symmetry. In both phases, the magnetic moment of Fe1 (and Fe2)

Table 1 | DFT deduced values of the magnetic moment in both spin orientations are presented in μ_B unit

Ions	cFM phase			nFM phase		
	$E = -32.094$ eV			$E = -32.083$ eV		
	m_x	m_y	m_z	m_x	m_y	m_z
Fe1, Fe2	0	0	2.8	1.6	1.6	1.7
Fe3, Fe4	0	0	3.2	1.0	1.0	2.7

Table 2 | Parameters obtained from the transport measurements

Properties	D16 (16 nm)	D95 (95 nm)	Bulk
RRR	3.87	3.04	1.31 [20] 1.75 [95]
Conductivity (σ) at T_C (Ω^{-1} m^{-1})	9.6×10^5	8.6×10^5	5×10^5 [20] 4.1×10^5 [95]
Conductivity (σ) at 1.6 K (Ω^{-1} m^{-1})	36.8×10^5	26.1×10^5	6.4×10^5 [20] 7.1×10^5 [95]
Coeff. of T^2 below T_Q (Ω cm K^{-2})	4.24×10^{-9}	7.73×10^{-9}	not reported
Coeff. of T^2 within 65 - 125 K (Ω cm K^{-2})	8.12×10^{-9}	2.41×10^{-9}	not reported
Negative MR (max) near T_{SR} (at 9 T)	21.2 %	11 %	not reported
Positive MR (max) below T_Q (at 9 T)	0.6 %	1.8%	not reported
$|\sigma_{xy}^{AHE}|$ at 10 K (Ω^{-1} cm^{-1})	155	121	495 [95]
$|\sigma_{xy}^{AHE}|$ (max) near T_{SR} (Ω^{-1} cm^{-1})	243	376	400 [95]
S_H (max) near T_{SR} (V^{-1})	0.15	0.24	0.0235 [20] 0.22 [95]
θ_H (max) near T_{SR}	0.015	0.032	0.028 [20] 0.106 [95]
Scaling parameter α	1.68	1.71	1.89 [95]
Coercive field near T_{SR} (Oe)	1050	270	negligible [20]

Comparison of several parameters deduced from the transport data of D16 and D95 with that reported for bulk F4GT [20,95].

is lower than that of Fe3 (Fe4). We refer to the first phase as collinear FM (cFM) and the second one by non-collinear FM (nFM). The quasi-degeneracy in the two reoriented spin configurations is responsible for the SR transition in this compound.

The band structure and the FS topology for the two phases are shown in Fig. 4d–g. We observe significant band structure differences near the Fermi level, with spectral weight redistribution as well as the appearance of new FS pockets in the nFM phase. Remarkably, all FSs are significantly 2D in nature, consistent with the vdW type interaction along the c-direction. In the cFM phase (see Fig. 4f), we have five FS pockets, four of which are hole-like while the fifth one is electron-like. On the other hand, in the nFM phase (see Fig. 4g), we find that two new FS pockets develop, with one of them being hole-like but much smaller in area, while the other one is electron-like and much larger in area. In addition, the area of all other FS pockets also increases. This result suggests that owing to the smaller magnetic moment of the Fe1 (and Fe2) compounds, the itinerant characteristics of the Fe-orbitals are enhanced here. This is evident by the fact that the two-electron pockets are dominated by the Fe3 and Fe4 atoms, as shown in Fig. 4e. The appearance of the new electron pockets is consistent with the sign change in the Hall resistivity from positive to negative in the intermediate temperature region. In addition, in the nFM phase, the wider bandwidth of the bands leads to higher velocities for electrons near the Fermi level due to a larger range of available states for them to occupy. This wider range of available energy states reduces the likelihood of electron scattering events, resulting in a sharp drop in resistivity at T_{SR} in the nFM phase.

The DFT results indicate that the low-energy electronic states are dominated by Fe-d orbitals (hybridized with p-states of the Te atoms. Therefore, the effective low-energy model requires a multi-band tight-binding model. But with an eye to the active spin degrees of freedom, one starts with a multi-band Hubbard model for two Fe-d orbitals with Hund's coupling, projects to the highest spin states in the ferromagnetic phase and obtain a Heisenberg model (where we suppress the charge degrees of free-dom for simplicity). The model Hamiltonian is

$$
\begin{aligned}
H = & -J_1 \sum_{<i,j>} \mathbf{s}_i \cdot \mathbf{s}_j - J_3 \sum_{<i,j>} \mathbf{S}_i \cdot \mathbf{S}_j \\
& - K_1 \sum_i (\mathbf{s}_i \cdot \hat{\mathbf{n}})^2 - K_3 \sum_i (\mathbf{S}_i \cdot \hat{\mathbf{N}})^2 \\
& - J' \sum_i \mathbf{S}_i \cdot \mathbf{s}_i.
\end{aligned}
\tag{7}
$$

Here $\mathbf{s}$, and $\mathbf{S}$ correspond to the spin vectors at the Fe1 and Fe3 atomic sites, with corresponding exchange and anisotropy interactions J_1, J_3, and K_1 and K_3, while J' is the inter-atomic exchange interaction. For $J' = 0$, the model enjoys spin-rotational symmetry for each Fe atom with respect to their easy axes $\hat{\mathbf{n}}$ and $\hat{\mathbf{N}}$, and a Ferromagnetic phase appears for $J_i > 0$ and $K_i \geq 0$. For $J' \neq 0$, the individual spin-rotational symmetry is lost, and a rotational symmetry with respect to the total spin $\mathbf{S} + \mathbf{s}$ with a common quantization axis is present.

Given that both phases are ferromagnetic along each Fe-layer, therefore the in-plane exchange terms $J_1 > 0$ and $J_3 > 0$, do play no role in the cFM to nFM phase transition. We rotate the spin-quantization axis by the polar angles $n_z = \cos(\theta_1)$ and $N_z = \cos(\theta_3)$ (with respect to the c-axis). Clearly, a trivial classical ferromagnetic solution exists at $\theta_i = 0$ for all values of J', which is the cFM phase.

Is there any other ferromagnetic order ($|\theta_3 - \theta_1| < \pi$) possible in the realistic parameter region in this model? The $\partial H / \partial \theta_i = 0$ condition of the Hamiltonian in Eq. (7) yields $K_1 s^2 \sin 2\theta_1 = -K_3 S^2 \sin 2\theta_3$, where S and s are the spin magnitudes of Fe3 and Fe1. In the FM region ($|\theta_3 - \theta_1| < \pi$), the condition is satisfied for $K_1/K_3 < 0$ for any $J' \neq 0$. Furthermore, $\partial^2 H / \partial \theta_i^2 > 0$ condition for the energy minimum imposes $K_1 < 0$ and $K_3 > 0$ for $J' > 0$ and $\theta_i < \pi/4$, which is satisfied in the parameter range of $2|K_2|s \cos 2\theta_1 < |J'|S \cos(\theta_3 - \theta_1) < 2|K_3| \cos 2\theta_3$. This gives the nFM phase. The self-consistent DFT result gives $\theta_1 = 10^o$ and $\theta_3 = 71^o$ and $s = 1.7\mu_B$ and $S = 2.7\mu_B$ in this phase.

Due to the presence of an inter-atomic spin-spin exchange term J', there arises a temperature scale below which the spins in the lower-moment Fe-d states are screened and give rise to a metallic phase. This characteristic temperature is the $T_Q \sim k_B J'$ in this material.

Conclusions

In summary, a comprehensive magnetotransport study is presented in a quasi-two-dimensional van der Waals ferromagnet, F4GT, followed by the understanding of different magnetic and electronic phases through first-principle calculations. By combining various transport properties like resistivity, ordinary Hall effect, AHE, and MR from two exfoliated nanoflake devices, we have identified two electronic transitions specified by T_{SR} and T_Q. While T_{SR} was reported before, the second transition, T_Q, was not identified earlier. We do observe these two transitions in both devices, however, the values of the transport parameters are sensitive to the sample thickness. A comparison (Table 2) of various transport parameters can be drawn from our devices with that of the reported data on bulk single crystals.

While at low temperatures, below T_Q, resistivity is governed mainly by electron-electron scattering, the other inelastic scattering contributions, electron-magnon and electron-phonon, become significant in the inter-mediate temperature range ($T_Q < T < T_{SR}$). Beyond T_{SR}, electron-phonon scattering dominates the resistivity. Notably, both the RRR and the absolute value of the conductivity increase with the reduction of thickness. Our

analysis clearly indicates that the electron-magnon interaction is stronger in the thinner device, consistent with the larger negative MR near T_{SR}. For both devices, MR becomes positive below T_Q and the ordinary Hall coefficient exhibits a clear sign change in the vicinity of T_{SR} and T_Q. Finally, we observe significant AHE contribution in both devices, however, the AHE conductivity near T_{SR} reduces with decreasing thickness. While the low-temperature AHE possibly arises due to the intrinsic K-L mechanism, our analysis reveals the extrinsic side-jump mechanism arising from spin-flip electron-magnon scattering, is responsible for the strong temperature dependence of AHE in the intermediate temperature range. Theoretical calculations reveal that the difference in the environment of Fe1 and Fe3 atoms and the inter-atomic exchange coupling (J') are responsible for complex phases, which in turn leads to a FS reconstruction. Our study deciphers an intriguing connection between charge and spin degrees of freedom, important for fundamental understanding as well as for possible futuristic applications.

Methods

Fe_4GeTe_2 single-crystal growth

The high-quality single-crystal Fe_4GeTe_2 was grown by the standard CVT method along with I_2 as a transport agent. Here, we have used the mixture of highly pure (99.99%) Fe, Ge, and Te materials powder with a molar ratio of 5:1:2 in a high vacuum quartz tube, and this was heated for seven days at 725 °C. The resultant material was further inserted inside an evacuated quartz tube and placed in a gradient temperature-based horizontal furnace with temperatures 800 °C and 750 °C maintained on each end for seven days along with the transport agent I_2 (2 mg cc^{-1}). Tiny pieces of thin single crystals were collected from the cold end of the quartz tube, each one having the typical dimensions of $1.3 \times 1.3 \times 0.05$ mm^3. The details of the sample preparation are given in our earlier report[21].

Crystal characterizations

Basic characterizations like X-ray diffraction are performed on a freshly cleaved thin and shiny single-crystal of Fe_4GeTe_2[21]. The presence of very sharp (0 0 l) peaks in the diffraction pattern confirms that the flat plane of the crystal is perpendicular to the crystallographic c-axis with interlayer separation of 28.74 Å. Also, high-resolution transmission electron microscopy and energy-dispersive X-ray spectrum were performed[21] revealing good single-crystal quality.

Magnetization measurements

The magnetization measurements of the bulk Fe_4GeTe_2 crystal were performed at ambient pressure in a superconducting quantum interference device vibrating sample magnetometer (SQUID-VSM) (MPMS 3, Quantum Design, USA) with the magnetic field applied along both out-of-plane and in-plane directions. Before starting the measurement, the remanence of the sample and the superconducting coil was removed by applying a magnetic field to 5 T and then by making it zero with oscillating mode. For each magnetization isotherm in M-B curves, the temperature was stabilized for around 25 min, and data were collected at different stable magnetic fields. The temperature-dependent dc magnetization was measured in the zero-field-cooled (ZFC) condition for the applied magnetic field of $B = 0.5$ kOe and 0.1 kOe with B∥ab and B∥c crystallographic axis of Fe_4GeTe_2 crystal. For M-T curves, The data were taken with an interval of 0.25 K with a rate of temperature change of 0.5 K min^{-1}.

Device fabrication and magnetotransport measurements

As these ferromagnetic materials are sensitive in ambient conditions, we fabricated the Hall bar devices through the dry-transfer method on a pre-patterned Ti (10 nm)/Au (45 nm) contacts on a 285 nm SiO_2/Si(p++) substrate. First, we fabricate gold pads using optical lithography (LW405 by MICROTECH) and a lift-off process followed by oxygen plasma treatment (ICP-RIE unit by SENTECH 500) to clean the organic residues. Then we exfoliate thin layers of Fe_4GeTe_2 crystal by standard mechanical exfoliation on a thin polydimethylsiloxane (PDMS) layer and transferred onto the gold

pads at an elevated temperature (90 °C–110 °C) using a home-made dry-transfer set up. The device was then immediately coated with PMMA (microresist technology) e-beam resist to avoid any oxidation of the flake. The whole transfer process was completed within 30 minutes. The device was then bonded with silver paint (SPI supplies) and contacts were checked using SR830 lock-in and Keithley 2450 source meter. All the contacts were found to be ohmic. The in-plane resistivity, Hall coefficient, and other transport measurements are performed using standard lock-in techniques at frequency 234.1 Hz in a low-temperature magnetotransport setup (Teslatron, Oxford Instruments) in the temperature range: 1.6–300 K. The four-terminal resistivity (ρ_{xx}) is calculated from the measured resistance (R) using the formula, $\rho_{xx} = R \times (W \times t/L)$, where W is the width of the flake, t is the thickness of the flake and L is the distance between two longitudinal electrodes. To eliminate the longitudinal component due to small misalignment of the Hall electrodes, the Hall resistivity (ρ_{xy}) was measured by taking the data for both positive and negative magnetic fields and then taking the anti-symmetric components of the Hall resistivity by using the formula: $\rho_{xy}(B) = (\rho_{xy}(+B) - \rho_{xy}(-B))/2$.

Theoretical calculation and computational details

The DFT simulation was performed by using the Vienna Ab initio Simulation Package (VASP)[84,85]. For the exchange-correlation between electrons, the generalized gradient approximation (GGA) was employed and it was parametrized by Perdew–Burke–Ernzerhof[86]. The projector–augmented wave (PAW) approach was employed to characterize the interaction between the core and valence electrons[87,88]. The plane–wave energy cutoff is set at 400 eV. The Brillouin zone (BZ) is sampled using the Monkhorst–Pack technique[89] with a grid spacing of 0.01 for all calculations, which yields equivalent $29 \times 29 \times 29$ and $30 \times 30 \times 3$ k-point meshes for rhombohedral and hexagonal unit cells, respectively. The structural relaxation was carried out until the forces acting on each atom were less than 0.0001 eV/Å. The convergence threshold for energy in the electronic self–consistent cycle was set to 10^{-8} eV. The simplified method suggested by Dudarev et al.[90] was used to make the GGA + U calculations, which simply considers the difference of U and J ($U_{eff} = U - J$). The value of U_{eff} for Fe 3d was set at 4.0 eV[91], while it is zero for the other atoms. We also performed the spin–orbit coupling (SOC) calculations.

The Fe_4GeTe_2 crystal structure belongs to the space group $R\bar{3}m$ (No. 166). The position of the atoms was relaxed while maintaining the lattice constants at the experimental values[20,21] of $a = b = 4.044$ Å, and $c = 29.247$ Å for the hexagonal unit cell. The band structure and FS calculations were performed using the rhombohedral primitive cell (see Fig. 4a–c), which was generated using the VASPKIT code[92]. Fe atoms in the primitive cell are shown in different colors. All the crystal structures shown here were created using VESTA software[93].

Note added: After our submission[94], a recent work[95] focusing only on the AHE in a bulk Fe_4GeTe_2 single crystal is reported.

Data availability

The authors declare that the data, supporting the findings, are available within the paper and its Supplementary Information. The corresponding authors can also provide data upon reasonable request.

References

1. Huang, B. et al. Layer-dependent ferromagnetism in a van der Waals crystal down to the monolayer limit. *Nature* **546**, 270–273 (2017).
2. Gong, C. et al. Discovery of intrinsic ferromagnetism in two-dimensional van der Waals crystals. *Nature* **546**, 265–269 (2017).
3. Song, T. et al. Giant tunneling magnetoresistance in spin-filter van der Waals heterostructures. *Science* **360**, 1214–1218 (2018).
4. Klein, D. R. et al. Probing magnetism in 2D van der Waals crystalline insulators via electron tunneling. *Science* **360**, 1218–1222 (2018).

5. Burch, K. S. Electric switching of magnetism in 2D. *Nat. Nanotechnol.* **13**, 532–532 (2018).

6. McGuire, M. A., Dixit, H., Cooper, V. R. & Sales, B. C. Coupling of crystal structure and magnetism in the layered, ferromagnetic insulator CrI_3. *Chem. Mater.* **27**, 612–620 (2015).

7. Zhong, D. et al. Van der Waals engineering of ferromagnetic semiconductor heterostructures for spin and valleytronics. *Sci. Adv.* **3**, 1–7 (2017).

8. Samarth, N. Magnetism in flatland. *Nature* **546**, 216–217 (2017).

9. Zhang, W., Wong, P. K. J., Zhu, R. & Wee, A. T. S. Van der Waals magnets: wonder building blocks for two-dimensional spintronics? *InfoMat* **1**, 479–495 (2019).

10. Kim, S. J. et al. Interface engineering of magnetic anisotropy in van der waals ferromagnet-based heterostructures. *ACS Nano* **15**, 16395–16403 (2021).

11. Tan, C. et al. Hard magnetic properties in nanoflake van der Waals Fe_3GeTe_2. *Nat. Commun.* **9**, 1554 (2018).

12. Fei, Z. et al. Two-dimensional itinerant ferromagnetism in atomically thin Fe_3GeTe_2. *Nat. Mater.* **17**, 778–782 (2018).

13. Deng, Y. et al. Gate-tunable room-temperature ferromagnetism in two-dimensional Fe_3GeTe_2. *Nature* **563**, 94–99 (2018).

14. Kim, K. et al. Large anomalous Hall current induced by topological nodal lines in a ferromagnetic van der Waals semimetal. *Nat. Mater.* **17**, 794–799 (2018).

15. Fujita, R. et al. Layer-dependent magnetic domains in atomically thin Fe_5GeTe_2. *ACS Nano* **16**, 10545–10553 (2022).

16. Tan, C. et al. Gate-controlled magnetic phase transition in a van der Waals magnet Fe_5GeTe_2. *Nano Lett.* **21**, 5599–5605 (2021).

17. Alahmed, L. et al. Magnetism and spin dynamics in room-temperature van der Waals magnet Fe_5GeTe_2. *2D Mater.* **8**, 045030 (2021).

18. Deng, Y. et al. Layer-number-dependent magnetism and anomalous Hall effect in van der Waals ferromagnet Fe_5GeTe_2. *Nano Lett.* **22**, 9839–9846 (2022).

19. Bera, S. et al. Enhanced coercivity and emergence of spin cluster glass state in 2D ferromagnetic material Fe_3GeTe_2. *J. Magn. Magn. Mater.* **583**, 171052 (2022).

20. Seo, J. et al. Nearly room temperature ferromagnetism in a magnetic metal-rich van der Waals metal. *Sci. Adv.* **6**, 1–10 (2020).

21. Mondal, S., Khan, N., Mishra, S. M., Satpati, B. & Mandal, P. Critical behavior in the van der Waals itinerant ferromagnet Fe_4GeTe_2. *Phys. Rev. B* **104**, 094405 (2021).

22. Bera, S. et al. Unravelling the nature of spin reorientation transition in quasi-2D vdW magnetic material, Fe_4GeTe_2. *J. Magn. Magn. Mater.* **565**, 170257 (2023).

23. Wang, H. et al. Interfacial engineering of ferromagnetism in wafer-scale van der Waals Fe_4GeTe_2 far above room temperature. *Nat. Commun.* **14**, 2483 (2023).

24. Ershadrad, S., Ghosh, S., Wang, D., Kvashnin, Y. & Sanyal, B. Unusual magnetic features in two-dimensional Fe_5GeTe_2 induced by structural reconstructions. *J. Phys. Chem. Lett.* **13**, 4877–4883 (2022).

25. May, A. F., Bridges, C. A. & McGuire, M. A. Physical properties and thermal stability of $Fe_{5-x}GeTe_2$ single crystals. *Phys. Rev. Mater.* **3**, 104401 (2019).

26. Zhang, H. et al. Itinerant ferromagnetism in van der Waals $Fe_{5-x}GeTe_2$ crystals above room temperature. *Phys. Rev. B* **102**, 064417 (2020).

27. Liu, P. et al. Magnetic and magneto-transport studies in van der Waals $Fe_{5-x}GeTe_2$ flakes. *Appl. Phys. Lett.* **121**, 112402 (2022).

28. Mermin, N. D. & Wagner, H. Absence of ferromagnetism or antiferromagnetism in one- or two-dimensional isotropic Heisenberg models. *Phys. Rev. Lett.* **17**, 1133–1136 (1966).

29. Bander, M. & Mills, D. L. Ferromagnetism of ultrathin films. *Phys. Rev. B* **38**, 12015–12018 (1988).

30. Hook, J. & Hall, H. *Solid State Physics* (John Wiley & Sons, Ltd. Chichester, 1991).

31. Yi, J. et al. Competing antiferromagnetism in a quasi-2D itinerant ferromagnet Fe_3GeTe_2. *2D Mater.* **4**, 011005 (2017).

32. Wang, Q., Sun, S., Zhang, X., Pang, F. & Lei, H. Anomalous Hall effect in a ferromagnetic Fe_3Sn_2 single crystal with a geometrically frustrated Fe bilayer kagome lattice. *Phys. Rev. B* **94**, 1–5 (2016).

33. Kumar, N., Soh, Y., Wang, Y. & Xiong, Y. Magnetotransport as a diagnostic of spin reorientation: Kagome ferromagnet as a case study. *Phys. Rev. B* **100**, 1–7 (2019).

34. Biswas, A. et al. Spin-reorientation-induced band gap in Fe_3Sn_2: optical signatures of weyl nodes. *Phys. Rev. Lett.* **125**, 076403 (2020).

35. Fenner, L. A., Dee, A. A. & Wills, A. S. Non-collinearity and spin frustration in the itinerant kagome ferromagnet Fe_3Sn_2. *J. Phys. Condens. Matter* **21**, 452202 (2009).

36. Xiao, Y. et al. Spin-reorientation transition induced magnetic skyrmion in $Nd_2Fe_{14}B$ magnet. *Appl. Phys. Lett.* **117**, 132402 (2020).

37. Yin, J.-X. et al. Quantum-limit Chern topological magnetism in $TbMn_6Sn_6$. *Nature* **583**, 533–536 (2020).

38. Zajkov, N. K., Mushnikov, N. V., Bartashevich, M. I. & Goto, T. Magnetization processes in the $TbMn_6Sn_6$ compound. *J. Alloy. Compd.* **309**, 26–30 (2000).

39. Malaman, B. et al. Magnetic properties of RMn_6Sn_6 (R = Gd-Er) compounds from neutron diffraction and Mossbauer measurements. *J. Magn. Magn. Mater.* **202**, 519–534 (1999).

40. Clatterbuck, D. M. & Gschneidner, K. A. Magnetic properties of RMn_6Sn_6 (R = Tb, Ho, Er, Tm, Lu) single crystals. *J. Magn. Magn. Mater.* **207**, 78–94 (1999).

41. Wang, X. & Tan, J. Switching from extrinsic to intrinsic anomalous Hall effect around Lifshitz transition in a Kagome-lattice ferromagnet. *Appl. Phys. Lett.* **122**, 051901 (2023).

42. Chen, L. et al. Spin reorientation transition and negative magnetoresistance in ferromagnetic $NdCrSb_3$ single crystals. *Materials* **16**, 1736 (2023).

43. Aparnadevi, M. & Mahendiran, R. Electrical detection of spin reorientation transition in ferromagnetic $La_{0.4}Sm_{0.3}Sr_{0.3}MnO_3$. *J. Appl. Phys.* **113**, 17D719 (2013).

44. Mondal, S. & Mandal, P. Anomalous magnetic properties of quasi two-dimensional van der Waals ferromagnet Fe_4GeTe_2. *Preprint at* http://arxiv.org/abs/2207.09885 1–8 (2022).

45. Wang, X. & Tan, J. Intrinsic anomalous Hall effect and Lifshitz transition in a ferromagnetic kagome-lattice metal. *Appl. Phys. Lett.* **121** (2022).

46. Sau, J., Hassan, S. R., Kumar, N. & Kumar, M. Topological properties and anomalous transport in van der Waals ferromagnets Fe_nGeTe_2: a comparative study. *Phys. Scr.* **98**, 125916 (2023).

47. Ghosh, S., Ershadrad, S., Borisov, V. & Sanyal, B. Unraveling effects of electron correlation in two-dimensional Fe_nGeTe_2 (n=3, 4, 5) by dynamical mean field theory. *npj Comput. Mater.* **9**, 86 (2023).

48. Wang, Y. et al. Anisotropic anomalous Hall effect in triangular itinerant ferromagnet Fe_3GeTe_2. *Phys. Rev. B* **96**, 1–6 (2017).

49. Ke, J. et al. Magnetic and magneto-transport studies of two-dimensional ferromagnetic compound Fe_3GeTe_2. *J. Phys. Condens. Matter* **32**, 405805 (2020).

50. Jones, D. C. et al. Origin of spin reorientation and intrinsic anomalous Hall effect in the kagome ferrimagnet $TbMn_6Sn_6$. *Preprint at* https://arxiv.org/abs/2203.17246 (2022).

51. Saha, P., Singh, M., Nagpal, V., Das, P. & Patnaik, S. Scaling analysis of anomalous Hall resistivity and magnetoresistance in the quasi-two-dimensional ferromagnet Fe_3GeTe_2. *Phys. Rev. B* **107**, 35115 (2023).

52. Chen, B. et al. Magnetic properties of layered itinerant electron ferromagnet Fe_3GeTe_2. *J. Phys. Soc. Jpn.* **82**, 1–7 (2013).

53. Raquet, B., Viret, M., Sondergard, E., Cespedes, O. & Mamy, R. Electron-magnon scattering and magnetic resistivity in 3d ferromagnets. *Phys. Rev. B* **66**, 24433 (2002).

54. Jena, R. P., Kumar, D. & Lakhani, A. Scaling analysis of anomalous Hall resistivity in the Co_2TiAl Heusler alloy. *J. Phys. Condens. Matter* **32**, 365703 (2020).

55. Behnia, K. On the Origin and the Amplitude of T-Square Resistivity in Fermi Liquids. *Ann. Phys.* **534**, 2100588 (2022).

56. Klein, L. et al. Anomalous spin scattering effects in the badly metallic itinerant ferromagnet $SrRuO_3$. *Phys. Rev. Lett.* **77**, 2774–2777 (1996).

57. Lin, X., Fauqué, B. & Behnia, K. Scalable T^2 resistivity in a small single-component Fermi surface. *Science* **349**, 945–948 (2015).

58. Pariari, A. et al. Interplay between charge density wave order and magnetic field in the nonmagnetic rare-earth tritelluride $LaTe_3$. *Phys. Rev. B* **104**, 1–12 (2021).

59. Wang, J. et al. T-square resistivity without Umklapp scattering in dilute metallic Bi_2O_2Se. *Nat. Commun.* **11**, 1–8 (2020).

60. Roy, S., Khan, N. & Mandal, P. Unconventional transport properties of the itinerant ferromagnet $EuTi_{1-x}Nb_xO_3 (x = 0.10-0.20)$. *Phys. Rev. B* **98**, 134428 (2018).

61. Taylor, G. R., Isin, A. & Coleman, R. V. Resistivity of Iron as a Function of Temperature and Magnetization. *Phys. Rev.* **165**, 621–631 (1968).

62. Porter, N. A., Gartside, J. C. & Marrows, C. H. Scattering mechanisms in textured FeGe thin films: Magnetoresistance and the anomalous Hall effect. *Phys. Rev. B* **90**, 024403 (2014).

63. Pippard, A. B. *Magnetoresistance in metals* (Cambridge University Press, Cambridge, UK, 1989).

64. Khosla, R. P. & Fischer, J. R. Magnetoresistance in degenerate CdS: Localized magnetic moments. *Phys. Rev. B* **2**, 4084–4097 (1970).

65. Yosida, K. Magnetic Properties of Cu-Mn Alloys. *Phys. Rev.* **106**, 893–898 (1957).

66. Pugh, E. M. Hall effect and the magnetic properties of some ferromagnetic materials. *Phys. Rev.* **36**, 1503–1511 (1930).

67. Pugh, E. M. & Lippert, T. W. Hall e.m.f. and Intensity of Magnetization. *Phys. Rev.* **42**, 709–713 (1932).

68. Li, H. et al. Large anomalous Hall effect in a hexagonal ferromagnetic Fe_5Sn_3 single crystal. *Phys. Rev. B* **101**, 140409 (2020).

69. Lee, M., Onose, Y., Tokura, Y. & Ong, N. P. Hidden constant in the anomalous Hall effect of high-purity magnet MnSi. *Phys. Rev. B* **75**, 172403 (2007).

70. Nagaosa, N., Sinova, J., Onoda, S., MacDonald, A. H. & Ong, N. P. Anomalous Hall effect. *Rev. Mod. Phys.* **82**, 1539–1592 (2010).

71. Karplus, R. & Luttinger, J. M. Hall effect in ferromagnetics. *Phys. Rev.* **95**, 1154–1160 (1954).

72. Jungwirth, T., Niu, Q. & MacDonald, A. H. Anomalous Hall effect in ferromagnetic semiconductors. *Phys. Rev. Lett.* **88**, 207208 (2002).

73. Onoda, M. & Nagaosa, N. Topological Nature of Anomalous Hall Effect in Ferromagnets. *J. Phys. Soc. Jpn.* **71**, 19–22 (2002).

74. Berger, L. Side-jump mechanism for the Hall effect of ferromagnets. *Phys. Rev. B* **2**, 4559–4566 (1970).

75. Smit, J. The spontaneous Hall effect in ferromagnetics I. *Physica* **XXI**, 877–887 (1955).

76. Smit, J. The spontenous Hall effect in ferromagnets II. *Phys. (Amst.)* **24**, 39–51 (1958).

77. Liu, Y., Stavitski, E., Attenkofer, K. & Petrovic, C. Anomalous Hall effect in the van der Waals bonded ferromagnet $Fe_{3-x}GeTe_2$. *Phys. Rev. B* **97**, 165415 (2018).

78. Nozieres, P. & Lewiner, C. A simple theory of the anomalous Hall effect. *J. Phys. (Paris)* **34**, 901 (1973).

79. Tian, Y., Ye, L. & Jin, X. Proper scaling of the anomalous Hall effect. *Phys. Rev. Lett.* **103**, 1–4 (2009).

80. Miyasato, T. et al. Crossover behavior of the anomalous Hall effect and anomalous Nernst effect in itinerant ferromagnets. *Phys. Rev. Lett.* **99**, 86602 (2007).

81. Yang, S. A., Pan, H., Yao, Y. & Niu, Q. Scattering universality classes of side jump in the anomalous Hall effect. *Phys. Rev. B* **83**, 125122 (2011).

82. Wang, P. et al. Sign change of competing contributions to the side jump by impurity, phonon, and magnon scattering. *Phys. Rev. B* **107**, 094418 (2023).

83. Markou, A. et al. Thickness dependence of the anomalous Hall effect in thin films of the topological semimetal Co_2MnGa. *Phys. Rev. B* **100**, 054422 (2019).

84. Kresse, G. & Furthmüller, J. Efficient iterative schemes for ab initio total-energy calculations using a plane-wave basis set. *Phys. Rev. B* **54**, 11169–11186 (1996).

85. Kresse, G. & Furthmüller, J. Efficiency of ab-initio total energy calculations for metals and semiconductors using a plane-wave basis set. *Comput. Mater. Sci.* **6**, 15–50 (1996).

86. Perdew, J. P., Burke, K. & Ernzerhof, M. Generalized gradient approximation made simple. *Phys. Rev. Lett.* **77**, 3865–3868 (1996).

87. Blöchl, P. E. Projector augmented-wave method. *Phys. Rev. B* **50**, 17953–17979 (1994).

88. Kresse, G. & Joubert, D. From ultrasoft pseudopotentials to the projector augmented-wave method. *Phys. Rev. B* **59**, 1758–1775 (1999).

89. Monkhorst, H. J. & Pack, J. D. Special points for Brillouin-zone integrations. *Phys. Rev. B* **13**, 5188–5192 (1976).

90. Dudarev, S. L., Botton, G. A., Savrasov, S. Y., Humphreys, C. J. & Sutton, A. P. Electron-energy-loss spectra and the structural stability of nickel oxide: An LSDA+U study. *Phys. Rev. B* **57**, 1505–1509 (1998).

91. Guo, Y., Zhao, Y., Zhou, S. & Zhao, J. Oxidation behavior of layered Fe_nGeTe_2 (n = 3, 4, 5) and $Cr_2Ge_2Te_6$ governed by interlayer coupling. *Nanoscale* **14**, 11452–11460 (2022).

92. Wang, V., Xu, N., Liu, J.-C., Tang, G. & Geng, W.-T. VASPKIT: a user-friendly interface facilitating high-throughput computing and analysis using VASP code. *Comput. Phys. Commun.* **267**, 108033 (2021).

93. Momma, K. & Izumi, F. VESTA 3 for three-dimensional visualization of crystal, volumetric and morphology data. *J. Appl. Crystallogr.* **44**, 1272–1276 (2011).

94. Pal, R., Pal, B., Mondal, S., Mandal, P. & Pal, A. N. Unusual magnetotransport and anomalous Hall effect in quasi-two-dimensional van der Waals ferromagnet Fe_4GeTe_2. *Preprint at* https://arxiv.org/abs/2303.07440 1-10 (2023).

95. Bera, S. et al. Anomalous Hall effect induced by Berry curvature in topological nodal-line van der Waals ferromagnet Fe_4GeTe_2. *Phys. Rev. B* **108**, 115122 (2023).

Acknowledgements

Author contributions

A.N.P. and R.P. conceived the project. R.P. and B.P. designed the experiments. R.P. fabricated the devices and performed the characterization. R.P. and B.P. performed the detailed transport measurements. R.P. performed the complete data analysis. S.M. and P.M.

have grown and characterized the single crystal. R.S. and T.D. provided theoretical support and wrote the theoretical part. R.P. wrote the original manuscript. A.N.P. and P.M. supervised the project, validated the analysis, and reviewed and edited the manuscript. All authors have approved the final version of the manuscript.

Competing interests

The authors declare no competing interests.

Additional information

Publisher's note Springer Nature remains neutral with regard to jurisdictional claims in published maps and institutional affiliations.